Performance limiting factors in anode-supported cells originating from metallic interconnector design

Michael Kornely [a,*], André Leonide [a], André Weber [a], Ellen Ivers-Tiffée [a,b]

[a] Institut für Werkstoffe der Elektrotechnik (IWE), Karlsruher Institut für Technologie (KIT), Adenauerring 20b, 76131 Karlsruhe, Germany
[b] DFG Center for Functional Nanostructures (CFN), Karlsruhe Institute of Technology (KIT), 76131 Karlsruhe, Germany

ABSTRACT

The combination of advanced characterization techniques and FEM-simulations provided detailed information about losses related to the flowfield geometry of a metallic interconnector (MIC) in a planar SOFC repeat unit. The presented 2-D FEM model is able to predict the repeat unit performance decrease due to the in plane ohmic losses in the electrodes and the contact resistance between electrode and MIC.

The performed calculation and measurement showed an increase of ohmic losses of up to 84% when the single cell was contacted with a MIC, The contact resistance adds less than 6% on the cathode side. The in-plane current flow from the contact ribs to the triple phase boundaries under the gas channels caused 94% of the additional ohmic losses.

Analysis of impedance spectra by the distribution of relaxation times and a subsequent Complex Nonlinear Least Squares fit separated gas diffusion from the total polarization losses. Depending on flowfield design, the gas diffusion resistance on the cathode side increased up to +750%.

For high-performance anode supported cells, the choice of cathode flowfield design added up to 41% power loss, whereas the anodic flowfield design was of minor importance (<1% power loss).

© 2010 Elsevier B.V. All rights reserved.

1. Introduction

The performance of high temperature solid oxide fuel cells (SOFC) at the single-cell level has been continuously improved over the past 10 years [1]. However, at the stack level, the power density becomes unprofitable by a decrease of 50% [2]. A search for the causes leads to the part of the metallic interconnector (MIC). Apart from chromium poisoning of the cathode [3–5], additional losses caused by the MIC geometry [6] reduce the cell performance. Herein, additional ohmic and polarization losses are created by the flowfield geometry, in particular (i) non ideal contacting through contact resistance or limited contact area and (ii) limited gas delivery through gas channels.

Different models of repeating units were proposed to investigate the impact of MIC design on the performance of solid oxide fuel cells (SOFC). Nelson et al. provided a continuum-level model by analyzing the effects of (i) constriction resistance, (ii) contacting to mass transport, and (iii) fuel depletion at the triple phase boundaries (TPB) [7]. Tanner and Virkar gave an analytical expression for the ohmic area-specific resistance (ASR_0) of a repeat unit. They used differential elements considering expressions for charge transfer resistance, electrical conductivities, electrostatic potential, and MIC geometry [8]. A time dependent model was proposed by Gazzarri and Kessler to simulate the impedance spectra of a repeat unit. They developed AC and DC mass- and charge transport equations and combined them with the gas diffusion and the concentration polarization within the electrodes [6].

Previously published modeling attempts [6–8] present complex physical equations with a large quantity of parameters, which are difficult to determine by experiment. In contrast, the 2D FEM model presented here is based on experimental data extracted from (i) anode supported single cell performance and (ii) electrical conductivities of the applied materials. The 2D FEM model calculates (a) the current density and (b) the electrical potential distribution of a planar stack repeat unit (MIC/contact/ASC/contact/MIC). This numerical model can be adapted to other cell designs, and flowfield geometries.

2. FEM-model

The cross section of applied test setup shown in Fig. 1. In this study we investigated ideal contact conditions (a) and several test set ups with non ideal contact conditions of a repeat unit (b). It is obvious that test setup B comes closer to the contact conditions applied in a stack. Additional losses are expected here due to (i) the

* Corresponding author. Tel.: +49 721 6088456; fax: +49 721 6087492.
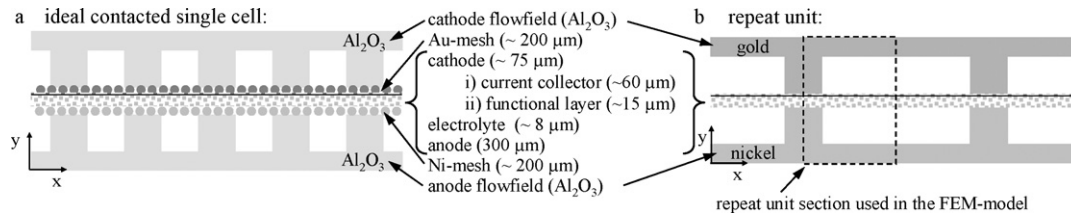 *E-mail address:* Michael.kornely@kit.edu (M. Kornely).

Fig. 1. Cross sections of the test setups with an ideal contact conditions (a) and a non ideal contact conditions (b). The single repeat unit displayed in (b) exhibited a contact rib width of 1 mm and a gas channel width of 4 mm.

contact resistance between electrode and flowfield, (ii) the in plane conduction in the electrodes as well as (iii) the gas transport in the thin cathode layer beneath the contact rib.

It has to be emphasized, that the transport processes (electronic and ionic current) and the electrochemical reactions have been converted into a purely electric steady state model. Furthermore, the in-plane gas diffusion below the contact ribs is not considered. The 2D model was implemented in the finite elemente methode software COMSOL Multiphysics V3.5 (COMSOL Inc., Burlington, USA). The discretisation of the cell and contact geometry was performed by the automatic mesh generator of COMSOL without local mesh refining. Altogether 5400 triangular elements were generated. The solving process of a current/voltage (*CV*) curve (0. . .2 A cm^{-2}, step size 20 mA cm^{-2}) takes not more than 45 s in a conventional workstation.

2.1. Geometry

The repeat unit shown in Fig. 1(b) represents the geometric contact conditions of a single cell. The ASC is in between two flowfields, comprises of both gas channels and contact ribs which included in the interconnector plates. The following assumptions are made: (1) the contact between the electrodes and the contact rib are homogeneous along the gas flow direction. The geometries of gas channels run parallel to the contact ribs and were constant in the gas flow direction. (2) The model represents an infinite cell element in the direction of the gas flow. Therefore the gas utilization can be neglected. (3) The geometry of each gas channel and contact rib is equal. As a consequence, a 2D-model considering just 1/2 of the contact rib (center of the contact rib at $x = 0$) and 1/2 of the gas channel (center of the gas channel at $x = L$) in x-direction describes the impact of the flowfield design on the cell performance (Fig. 2).

Equations and boundary conditions: The model consists of 4 sub domains: the anode (anode substrate + anode functional layer), the two layered cathode, and one MIC per electrode. The sub domains are implemented as electrical conductive sub-domains (Fig. 2a). The electric charge transport within the domains is described by the 2D Laplace equation with Neumann boundary condition (no internal species generation):

$$-\nabla(\sigma_d \nabla V_d) = 0 \qquad (1)$$

where σ_d is the electronic conductivity and V_d the electric potential in the sub-domain. The boundary conditions are defined as follows:

(1) The current is impressed as a current source/sink at $y = 0$ and $y = h$. The electrical potential in the MIC at $y = 0$ and $y = h$ is constant.
(2) Electric isolation for the symmetry divisions, i.e. no current flow in x-direction at $x = 0$ and $x = L$.

Eq. (2) describe the total current flow I_{ru} per repeat unit and Eq. (3) is used to calculate the total voltage loss U_{loss} per repeat unit.

$$I_{ru} = \int_A J_y dA = z \int_0^L j_{cell}(x)\big|_{y=c} dx \qquad (2)$$

$$U_{loss} = \int_0^h \vec{E}(y) dy \qquad (3)$$

2.2. Cell

The complex electrochemical reactions and the transport processes of an ASC are represented by its area specific resistance (ASR) in the electrical FEM-model. The open circuit voltage (corresponding to the oxygen activity gradient between the oxidant (air) and the fuel (H$_2$, 5% H$_2$O)) is not considered here because only the voltage losses U_{loss} of the repeat unit are of relevance. Current voltage (*CV*)-characteristics of the repeat unit ($U_{ru(I)}$), are simulated by subtraction of U_{loss} from the open circuit voltage OCV (Eq. (4)):

$$U_{ru}(I) = OCV - U_{loss}(I) \qquad (4)$$

An ASR-layer is inserted in between the electronically conducting cathode layer and the electronically conducting anode substrate (see Fig. 2, $y = c$). The ASR-layer represents the ohmic losses of the electrolyte and the electrodes as well as the polarization losses of the two electrodes [9]. This ASR-layer is implemented as a boundary condition in the COMSOL FEM model describing the local current density $j_{cell}(x)|_{y=c}$ flowing in y-direction through the ASR-layer $j_{cell}(x)$ as a function of the local electrical potential difference $\Delta U(x)|_{y=c}$ between cathode and anode at $y = c$. Both $j_{cell}(x)|_{y=c}$ and $\Delta U(x)|_{y=c}$ vary in the x-direction:

$$\Delta U(x)\big|_{y=c} = V_{cathode}(x)\big|_{y=c} - V_{anode}(x)\big|_{y=c} \qquad (5)$$

To parameterize the ASR-layer, CV-characteristics of an ideal contacted cell (see Fig. 1) have been used. A homogeneous current collection and gas distribution all over the active electrode areas is realized by a gold and a nickel contact mesh. Under these ideal conditions all transport processes (gas and bulk diffusion, electronic and ionic current flow) proceed in the y-direction. The ohmic resistance of the anode and the cathode in y-direction was calculated based on the 4-point measured conductivity of the porous electrode materials and the thickness of the layers. Due to the high conductivities (anode: 150 10^3 S m^{-1}, cathode: current collector 1300 S m^{-1}, functional layer 320 S m^{-1}) and the low thickness (anode: 300 μm, cathode: 75 μm) the ohmic resistance is fairly below 0.2 mΩ cm^2. In the end, the part of the ohmic losses in y-direction of theses layers in comparison with the sum of ohmic resistance of the electrolyte and the polarization losses of the electrodes can be neglected in case of the ideal contacting.

The total amount of ohmic and polarization losses of the ideal contacted cell are measured by *CV*-characteristics. Considering the ohmic losses in the electrodes in y-direction are negligible, the *CV*-
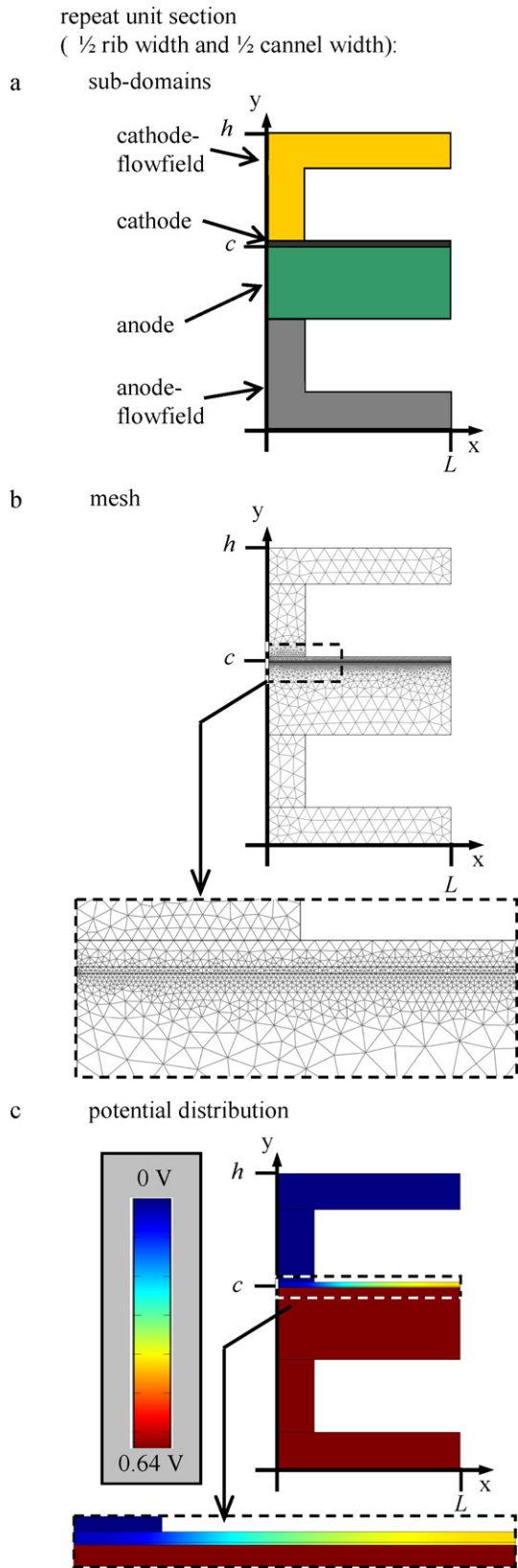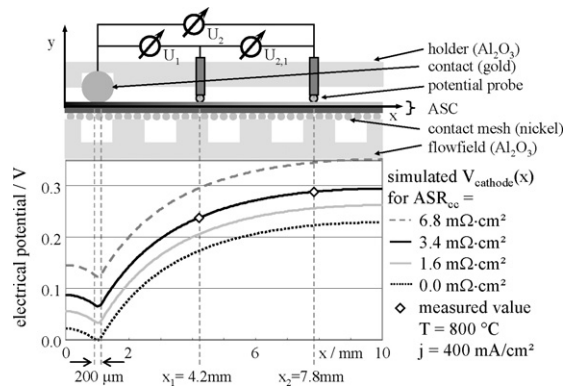
Fig. 3. Test geometry and calculated surface potential of the cathode for different ASR_{cc}-values. The potential difference between contact and surface potential includes the contributions of the contact resistance and the losses caused by in plane current flow. The measured values match with an ASR_{cc} of 3.4 mΩ cm^2 (T = 800 °C, $p(O_2)_{cathode}$ = 0.21 atm, $p(H_2O)_{anode}$ = 0.05 atm).

characteristic of the ideal contacted cell provides the ASR_{cell} as a function of the electrical potential difference ΔU at $y = c$:

$$ASR_{cell}(\Delta U) = \frac{\Delta U}{j_{cell}(\Delta U)} = \frac{OCV - U_{cell}}{j_{cell}(OCV - U_{cell})} \qquad (6)$$

The ASR_{cell} is only a function of the electrical potential difference ΔU at constant temperature and gas composition. The $ASR_{cell}(\Delta U)$ of the ideal contacted cell was implemented in the boundary condition between the cathode and the anode domain to calculate the local current density in y-direction through the ASR-layer:

$$j_{cell}(x)\Big|_{y=c} = \frac{\Delta U(x)\Big|_{y=c}}{ASR_{cell}\left(\Delta U(x)\Big|_{y=c}\right)} \qquad (7)$$

2.3. Contact resistance

The contact resistances in between MIC and both electrodes were likewise implemented as boundary conditions in between the concerned domains. In this study the area specific contact resistance in between gold-flowfield and cathode was directly evaluated from the repeat unit measurements. The simulated electrical potential distribution in the cathode was fitted to the electrical potential distribution measured by means of potential probes (Fig. 3) using the cathode contact resistance ASR_{cc} as the free fit parameter.

Total ohmic resistance: To calculate the total ohmic resistance of the repeat unit ($ASR_{0(ru)}$) the boundary condition (Eq. (7)) in between the cathode and anode sub domains were modified. The expression $ASR_{cell}(\Delta U)$ (Eq. (6)) is replaced by a constant resistance value which give the ohmic resistance of the electrolyte (Eq. (8)). The ASR_0 of the ideal contacted cell ($ASR_{0(ideal)}$) were determined by electrochemical impedance spectroscopy (EIS) and provide the ohmic resistance of the electrolyte and the negligible ohmic contribution of the electrodes as described above. The calculation of $ASR_{0(ru)}$ is carried out by the first Ohm's law (Eq. (9)):

$$j_{cell}(x)\Big|_{y=c} = \frac{\Delta U(x)\Big|_{y=c}}{ASR_{0(ideal)}} \qquad (8)$$

$$ASR_{0(ru)} = \frac{U_{loss}}{I_{(ru)}} \qquad (9)$$

3. Experimental

The ASCs within this study are based on 50 mm × 50 mm anode supported cells. The cosintered porous anode substrate (Ni/8YSZ-cermet), the anode functional layer (Ni/8YSZ-cermet) and the gas

Fig. 2. 2D FEM-Model geometry: the repeat unit section considered in the model consists of 1/2 of the contact rib and 1/2 of the gas channel. (a) Implemented sub domains, (b) mesh, (c) simulated electrical potential distribution.
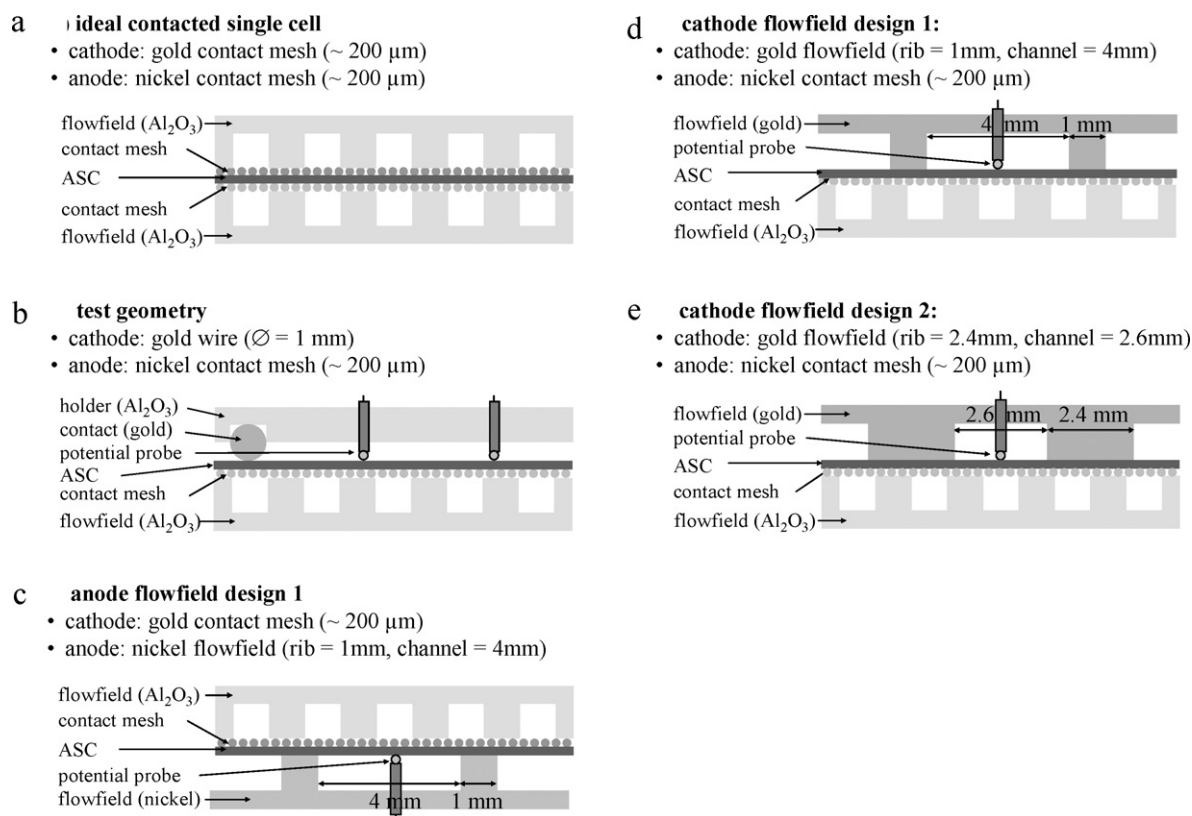
Fig. 4. Cross sections of the five different contact geometries applied in this study (a) ideal contact (provides ideal performance data), (b) test geometry (to validate the model) and (c), (d), (e) flowfields configuration (to investigate the limiting factors on performance of single cell).

tight electrolyte (8YSZ) were manufactured by CeramTec AG (Marktredwitz) [10]. Subsequently a double-layered $La_{0.65}Sr_{0.3}MnO_3$ (LSM, functional layer)/LSM-8YSZ (current collector) cathode was applied by screen printing and sintering. Details of the manufacturing procedures of the LSM-cathode can be found in [12]. The active area of the working cathode was 10 mm × 10 mm and two auxiliary (OCV probe) electrodes in gas flow direction in front of and behind the cathode [9]. ASCs and repeat units were tested in a single cell test bench [13] and characterized by CV- and EIS measurements.

Five different contact configurations were applied in this study, as displayed in Fig. 4: (a) ideal contact by a gold-mesh (cathode) and a nickel-mesh (anode) providing a homogeneous current collection and gas distribution, (b) a test geometry and (c), (d), (e) two flowfield designs distinguishable by contact rib width and gas channel width. The flowfields were made of gold to avoid corrosion effects at the cathode and nickel for the anode side, respectively.

Fig. 4(a) shows the ideal contacted single cell. This setup provides the ideal performance data ($ASR_{cell}(\Delta U)$) which was implemented in the model. The model was validated with the test geometry in Fig. 4b. The cathode was contacted in gas flow direction by a gold wire (1 mm diameter, 10 mm length) at $x = 5$ mm. The contact on the cathode side causes an in-plane current flow in the cathode in x-direction. The resulting voltage distribution was measured by two potential probes contacting the cathode surface at $x_1 = 4.2$ mm and $x_2 = 7.8$ mm, respectively (see also Fig. 3). The setups in Fig. 4(c)–(e) were used to investigate the cell performance depending on the flowfield geometry: (i) the anode was contacted by a nickel flowfield and the cathode was still ideal contacted (gold-mesh). The flowfield had a rib width of 1 mm and a channel width of 4 mm (see Fig. 4 c), (ii) the cathode was contacted by a gold flowfield and the anode by a nickel mesh. The dimension of the flowfield is rib width of 1 mm and a channel width of 4 mm (Fig. 4d). (iii) The cathode was contacted by a gold flowfield and the anode by a nickel

mesh. The dimension of the flowfield is a channel width of 2.6 mm and rib width of 2.7 mm, (Fig. 4e). The electrical potential was measured by potential probes, a spherical (~1 mm diameter) gold (cathode), respectively platinum (anode) contact, pressed against the electrode surface at a defined x-position (Figs. 4b–e and 3). The electrical potential at the electrode surface was evaluated by measuring the potential difference vs. a reference point, i.e. the gold respectively the nickel flowfield. The measured potential gives the sum of the voltage losses through the contact resistance and the voltage losses causes by the in plane current flow (x-direction).

The cells were operated under ambient pressure with different N_2/O_2 mixtures at the cathode side and varying H_2O/H_2 mixtures at the anode side. The total anodic and cathodic gas flow rates were maintained at a constant value of 0.25 ml min^{-1} during all experiments, resulting in a fuel utilization of 6% and an oxidant utilization of 12.6% at a current density of 2 A cm^{-2}. Additionally a mixture of 34% H_2, 45% N_2, and 21% H_2O by a lower gas flow rate of 199 ml min^{-1} were applied to investigate more realistic operation condition at the anode side. The cells were tested at an operating temperature of 800 °C. Potential probes measurements and performance data were carried out at constant current load and within CV-characteristic measurements. Impedance spectra were measured under open-circuit conditions with a Solartron 1260 frequency response analyzer in a frequency range from 100 mHz to 1 MHz. The amplitude of the current stimulus was adjusted in order to achieve a voltage response <12 mV. This procedure leads to a good signal-to-noise ratio (SNR) of the measured data and fulfils the condition of linearity in the operating point.

4. Results and discussion

Impact of the anode flowfield: The electrical potential difference between the anode substrate and the anode flowfield was
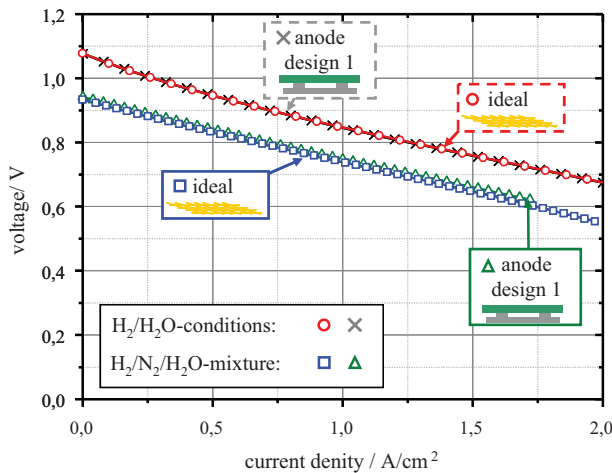
Fig. 5. Measured *C/V*-characteristics of applied anode contact geometries at different gas composition: (i) H_2 with 5% H_2O, and (ii) 34% H_2, 45% N_2, and 21% H_2O ($T = 800\,°C$).
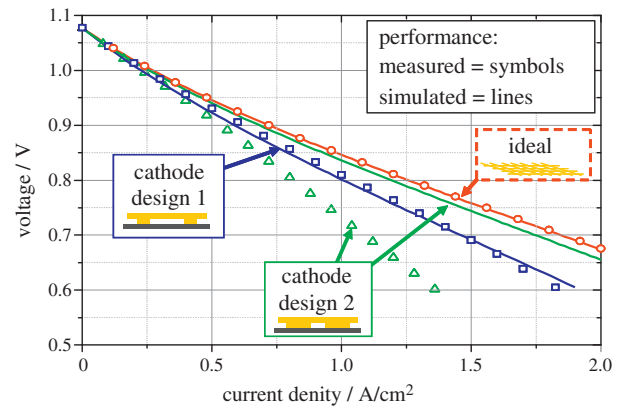

Fig. 6. Calculated (lines) and measured (symbols) *CV*-characteristics of an ideal contacted cell and the two cathode flowfield designs 1 and 2 ($T = 800\,°C$, $p(O_2)_{cathode} = 0.21$ atm, $p(H_2O)_{anode} = 0.05$ atm).

measured for two different anode contact geometries applying an ideal cathode contacting (Fig. 4(a) and (c)). The voltage loss related to the anode flowfield was always below 1 mV. The ASR-contribution of the in plane conduction (anode substrate and nickel flowfield) and the contact resistances (anode substrate/nickel-flowfield) was fairly below $1\,m\Omega\,cm^2$. This is in good agreement with the simulation results (Fig. 2c), the simulated and measured potential difference between the anode substrate and the anode flowfield was only 0.2 mV. Due to its high electronic conductivity the electrical potential within the anode substrate and the flowfield is nearly constant. A comparative analysis of *CV*-characteristics (Fig. 5) and impedance spectra of an ideal contacted cell (cathode: gold mesh, anode: nickel mesh) and of a cell with ideal contacted cathode (gold mesh) and a nickel flow field at the anode side showed neither any difference in performance nor in the polarization (measured) or the ohmic (measured and calculated) resistance (Table 1).

These measurements were carried out for a $p(H_2O)$ in the fuel (H_2) of 5% and a mixture of H_2, N_2, and H_2O to consider more realistic stack operation conditions. The experimental and modelling results showed that the anode flowfield geometry investigated in this study has a negligible impact on the cell performance (Fig. 5).

However, an anode flowfield with a larger contact rib width would further decrease the ohmic resistance but increase the gas diffusion polarization. Nevertheless, this would not improve the performance of the repeat unit significantly, because the ohmic losses are already close to zero ($<1\,\Omega\,cm^2$). These calculations and considerations clearly explain why no further experimental and modelling studies were carried out for the anode flowfield design. Fig. 5 shows the *C/V*-characteristics of ideal contacted cathode and both anode contact designs (ideal, flowfield design 1) for a $H_2/N_2/H_2O$ and H_2/H_2O conditions, respectively. These performance measurements confirm that the impact of the applied anode flowfield design is negligible for a wide range of fuel gas compositions. Naturally, the anode flowfield design has to be reconsidered when a more realistic fuel gas, as natural gas or as diesel reformate will be examined.

Application of potential probes: The test geometry was used to measure the electrical potential distribution at the cathode surface. By means of the two potential probes the contact resistance ASR_{cc} between the gold contact wire and the cathode was identified. The diagram in Fig. 3 shows the simulated electrical potential $V_{cathode}(x)$ of the cathode surface ($y = c + 75\,\mu m$) for different ASR_{cc}-values. Because all of the other parameters in the model are fixed, the con-

tact resistance ASR_{cc} can be evaluated by adapting the simulated electrical potential distribution of the cathode to the measured one. In case of a contact resistance of $ASR_{cc} = 3.4\,m\Omega\,cm^2$ the simulated electrical potential fully agrees with the measured values at $x_1 = 4.2$ mm and $x_2 = 7.8$ mm. The application of a potential probe in combination with the FEM-model enabled us to evaluate the contact resistance between electrode and flowfield in situ during the cell measurements. No additional contact resistance measurement is required to determine this value.

The potential difference between position x_1 and x_2 at the cathode surface remains unaltered during ASR_{cc} variation (Fig. 3). Thus, $V_{2.1}$, the difference in electrical potential of the cathode surface between position x_1 and x_2, is independent of the contact resistance and results solely from a voltage drop owing to the in-plane current flow parallel to the cathode/electrolyte interface (and, therefore, also between x_1 and x_2). This in-plane current is reduced by the current flow across the boundary into the electrolyte. Eq. (7) facilitates a spatially resolved calculation of the current density through the electrolyte as a function of the boundary condition ASR_{cell} (Eq. (6)). The very good agreement between measured and simulated values of $V_{2.1}$ shows that the simulated current density in the cathode and, thus, the model as a whole is able to precisely describe the current density distribution in the cathode depending on the contact geometry.

Impact of the cathode flowfield design: In Fig. 6 the simulated and the measured CV characteristics are shown for an ideal contacted cell as well as for the two analyzed cathode flowfield designs. In case of flowfield design 1 the measured performance ($P_{design1(0.7\,V)} = 1.03\,W\,cm^{-2}$) is decreased by 21%, as compared to the ideal contacted cell ($P_{ideal(0.7\,V)} = 1.3\,W\,cm^{-2}$). The flowfield design 2 caused a performance decrease of up to 41% ($P_{design2(0.7\,V)} = 0.76\,W\,cm^{-2}$). Measured and simulated values for the ideal contacted cell are in excellent agreement. This result confirms that the model correctly simulates the CV characteristics. Measured and simulated values for the flowfield design 1 show a rather small deviation varying with current density (error < 3%). At low current densities the measured values are slightly above the simulated whereas at high current densities the simulated voltage exceeds the measured. Measured and simulated values for the flowfield design 2 show a severe deviation. Moreover, the simulations result in a superior *CV*-characteristic for flowfield design 2, whereas the measurements show a superior *CV*-characteristic for flowfield design 1. The deviation between the model and the experimental values show a nonlinear increase with increasing current density.

Measured and calculated $ASR_{0(ru)}$ are shown in Table 1, and in Fig. 7. The values are in good agreement for the ideal contacted cell and both cathode flowfield designs. In case of design 1 and 2

Table 1
Calculated and measured ohmic resistance ASR0 and the measured polarization resistance ASRpol of an ideal contacted cell, the anode flowfield design 1, and the two cathode flowfield designs 1 and 2 at OCV-condition ($T = 800 °C$, $p(O_2)$cathode = 0.21 atm, $p(H_2O)$anode = 0.05 atm).

	Cathode	Anode	ASR_0 [mΩ cm^2]		ASR_{pol} [mΩ cm^2]
			Measured	Calculated	Measured
Ideal contact			34	34	316
Anode design 1			34	34	315
Cathode design 1			63	64	318
Cathode design 2			42	42	355

the contact resistance ASR_{cc} is below $2 m\Omega cm^2$. The total increase of ASR_0 (design 1 = 87%, flowfield design 2 = 24%) is mainly caused by the in-plane current flow from the contact ribs to the triple phase boundaries (TPB) under the gas channels (design 1 = 94%, design 2 = 87%). Due to the channel width the $ASR_{0(design\ 2)}$ is lower than $ASR_{0(design\ 1)}$ whereas the performance displayed an opposing dependency. This is a strong evidence for a further performance limiting factor (Fig. 7).

Fig. 8 shows the simulated cathode potential distribution $V_{cathode}(x)$ of the cathode surface ($y = c + 75\ \mu m$) and the related current density distribution $j_{cell(x)}|_{y=c}$ for different current loads in case of flowfield design 2. Using the procedure described above, an ASR_{cc} of $1 m\Omega cm^2$ was determined for a current density of $20 mA cm^{-2}$. Because the ASR_{cc} does not depend on the current density, this value should be applicable for all simulations.

With increasing current density the measured value of $V_{cathode}(x = 5 mm)$ slightly exceeds the simulated values. This indicates that the simulated current density in the gas channel is too low and/or the simulated current density under the contact ribs is too high. Considering that a constant current density under the contact ribs requires a homogeneous supply of O_2 the in-plane gas diffusion under the contact rib has to be considered. The in-plane gas diffusion path to the TPB under the contact area (max. $1200\ \mu m$) is significantly longer than in the case of the ideal contacted cell (only vertical gas diffusion, $\sim 75\ \mu m$) and causes additional losses. Therefore the assumption of negligible in-plane gas diffusion is a probable reason for the deviations described above.

To further analyze this, impedance spectra at different oxidant gas compositions (0.5–21% O_2 in N_2) were measured. The impedance measurement and data analysis was carried out according to the method described in of our previous papers [9,10]. As it can be seen in the distribution of relaxation times (DRT) [11] (Fig. 9a)) the gas diffusion process P_{1C} and the oxygen reduction process P_{2C} increase with decreasing $p(O_2)_{cathode}$. The gas diffusion resistance $R_{D(cathode)}$ was obtained for low $p(O_2)_{cathode}$ (<2%) by a CNLS fit using the equivalent circuit depicted in Fig. 9b) [9]. A direct evaluation of $R_{D(cathode)}$ from an impedance spectra

measured in air/H_2 (5% H_2O) is impossible because the small gas diffusion process P_{1C} at the cathode ($R_{D(cathode)}$(air) < $5 m\Omega \cdot cm^2$, relaxation frequency $\sim 9 Hz$) is hidden by the gas diffusion process P_{1A} in the anode substrate ($R_{1A} = 130 m\Omega cm^2$, relaxation frequency $\sim 4 Hz$). By well selected operating conditions, namely a high $p(H_2O)$ at the anode (63% H_2O) and a low $p(O_2)$ at the cathode (0.4...8%), R_{1A} is decreased to $30 m\Omega cm^2$, $R_{D(cathode)}$ increases and the relaxation frequency of P_{1C} is shifted to lower values. In this case the resistance R_{1A} was kept fixed during the entire fit procedures. Eq. (10) was used to calculate the $R_{D(cathode)}$ in air [14]. This equation describe the gas diffusion resistance in porous electrodes for a perfect one-dimensional diffusion (y-direction) in dependency of the $p(O_2)_{cathode}$, the temperature, and structure parameters.

In Fig. 9(c) $R_{D(cathode)}$ is displayed for the ideal contacted cell and the two flowfield designs. It is obvious that the $R_{D(cathode)}$-values and their $p(O_2)$-dependencies are significantly influenced by the flowfield design. The gas diffusion resistance increases with increasing contact rib width. Due to the increase in plane gas diffusion under the wide contact ribs (x-direction) the $p(O_2)$-dependence could not further describe by Eq. (10) [14], which assumes a one-dimensional gas diffusion. Due to this the $R_{D(cathode)}$ in air in case of wide ribs was calculated by a linear extrapolation of the fitted values.

$$R_{D(cathode)} = \left(\frac{RT}{4F}\right)^2 l_c \frac{1}{D_{O_2,N_2}} \frac{\tau_c}{V_{V,c}} \left(\frac{1}{p(O_2)_{cathode}} - 1\right)$$
$$\left(1.0133 \times 10^5 \frac{Pa}{atm}\right)^{-1} \tag{10}$$

The change in $p(O_2)$-dependence, which was observed in case of the flowfield design 2 (wide contact ribs), has to be attributed to a coupling of the in plane gas diffusion resistance in the cathode layer and the area specific resistance of the cell.

These results indicate for the cathode side, that the in plane gas diffusion below the contact rib must be considered. Obviously, the FEM-model of the repeat unit, which does not include in-plane gas diffusion under the contact ribs, is insufficient for a contact rib
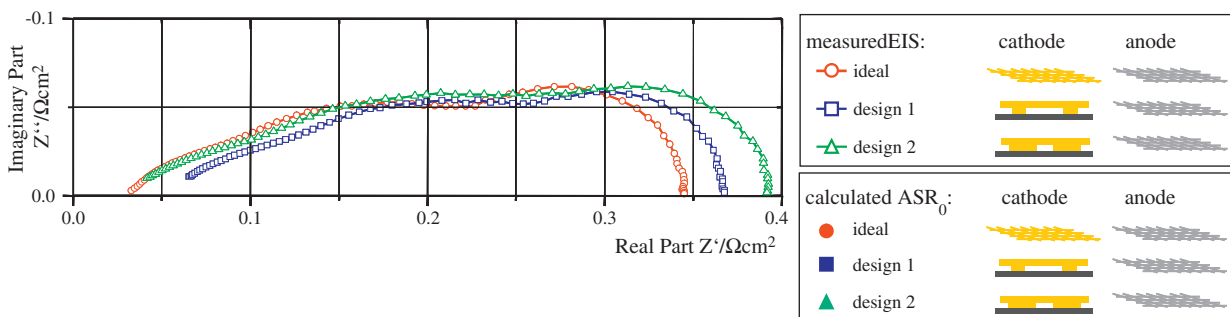

Fig. 7. Calculated $ASR_{0(ru)}$ (filled symbols) and measured EIS spectra of an ideal contacted cell and the two cathode flowfield designs 1 and 2 at OCV-condition ($T = 800 °C$, $p(O_2)_{cathode} = 0.21$ atm, $p(H_2O)_{anode} = 0.05$ atm).
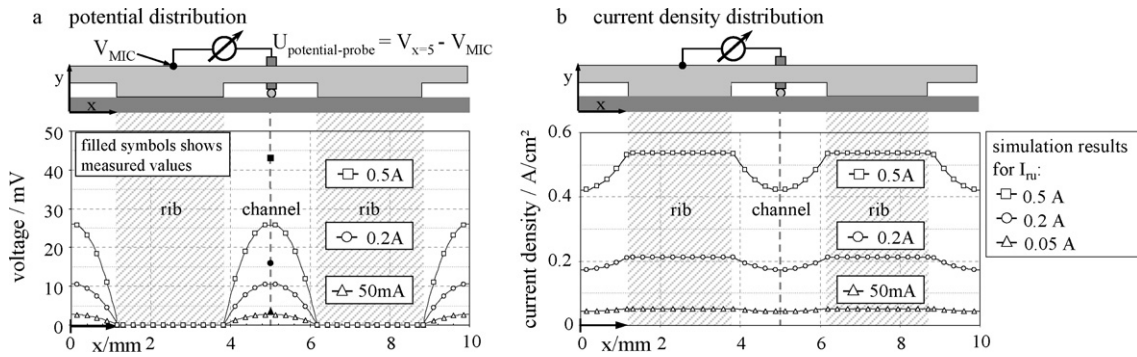
Fig. 8. Simulated potential $V_{cathode}(x)$ (a) and current density $j_{cell}(x)|_{y=c}$ (b) distribution for different currents I_{ru} ranging from 100 mA to 0.8 A for cathode flowfield design 2. The measured values $V_{cathode}$ ($x = 5$ mm) are displayed as filled symbols ($T = 800\,°C$, $p(O_2)_{cathode} = 0.21$ atm, $p(H_2O)_{anode} = 0.05$ atm).
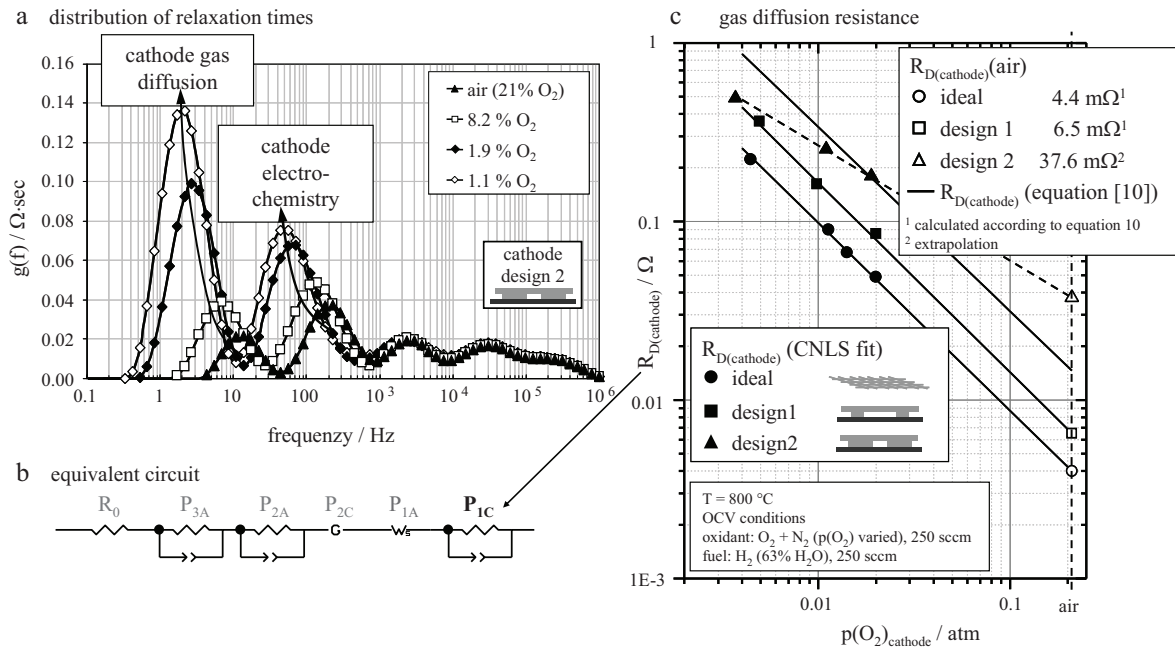

Fig. 9. (a) Distribution of relaxation times corresponding to measured impedance data ($T = 800\,°C$, OCV-condition, pO_2(cathode) = 0.011, ..., 0.21 atm, pH_2O(anode) = 0.05 atm). For cathode flowfield design 1, (b) equivalent circuit model with cathode gas diffusion process P_{1C} highlighted, and c) gas diffusion resistance $R_{D(cathode)}(p(O_2)_{cathode})$ for the ideal contacted cell and the two cathode flowfield designs.

width exceeding 1 mm. In this case, in-plane gas diffusion in the cathode layer must be integrated in the FEM model.

In Fig. 10 the ohmic resistance ASR_0 and the gas diffusion resistance $R_{D(cathode)}$ is displayed for the ideal contacted and the two flowfield designs. The increase in ASR_0 and $R_{D(cathode)}$, which is related to the electrical conduction beneath the gas channel and the gas diffusion beneath the contact ribs, respectively, correspond with the different contact rib and gas channel width of the 2 cathode flowfield designs.

Our experiments and the FEM-model show an increase of ohmic losses of 84%, when the cathode is contacted by a MIC with narrow contact ribs (design 1: 1 mm contact rib width, 4 mm gas channel width). The increase in ohmic losses is narrowed down to +24%, when the cathode is contacted by a MIC with wide contact ribs (design 2: 2.4 mm contact rib width, 2.6 mm gas channel width). This observation cannot be explained by the contact resistance between MIC and cathode, as it was less than 3% (3.4 mΩ cm²). Fact is that the in-plane current flow from the contact ribs to the triple phase boundaries is responsible for these ohmic contributions. As the MIC with wide contact ribs (design 2) has a smaller gas channel width (2.6 mm), the in-plane ohmic losses in the cathode are smaller. This part of the ohmic losses is governed by (i)
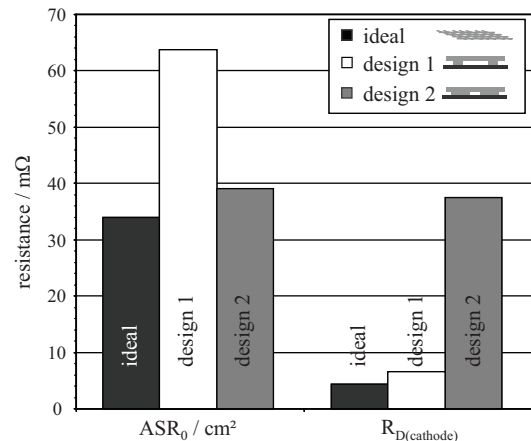

Fig. 10. Increase of the ohmic resistance ASR_0 and the gas diffusion resistance $R_{D(cathode)}$ for the two flowfield designs. In case of design 2 the $R_{D(cathode)}$ increase about 750% ($T = 800\,°C$, OCV condition pO_2(cathode) = 0.21 atm, pH_2O(anode) = 0.63 atm).

thickness and (ii) electronic conductivity of the cathode. As a consequence, the performance of the repeat unit can be increased by layout and/or materials choice.

Based on our experiments at OCV conditions, the gas diffusion resistance increased by 48% for the flowfield design with narrow contact ribs (design 1: 1 mm contact rib width, 4 mm gas channel width). As the ideal contacted cell exhibits a diffusion resistance of $4.4\,m\Omega\,cm^2$, this increase would correspond to $6.5\,m\Omega\,cm^2$ only. In contrast to this, in case of wide contact ribs (design 2: 2.4 mm contact rib width, 2.6 mm gas channel width) the increased diffusion resistance (+750%) leads to a remarkably high value of $37.5\,m\Omega\,cm^2$.

5. Conclusions

The combination of advanced characterization techniques and FEM-simulations provided detailed information about losses related to the flowfield geometry of a MIC in a planar SOFC repeat unit. The 2D FEM model developed in this study is able to predict the repeat unit performance decrease due to the in plane ohmic losses in the electrodes and the contact resistance between electrode and interconnector. Appropriate analysis of impedance data in combined with a calculation of the distribution of relaxation times (DRT) separated the gas diffusion losses below the contact ribs from the total polarization losses. Experimental and modeling results showed that the flowfield design on the cathode side had a large effect on the repeat unit performance whereas the flowfield design on the anode did not influence the performance under the testing conditions applied in this study.

The higher resistance of a repeat unit has to be attributed to in-plane transport processes in the cathode layer: (i) in-plane ohmic losses underneath the gas channels, which increase with gas channel width and (ii) in-plane gas diffusion losses underneath the contact ribs which increase with contact rib width. As a consequence, the best flowfield design was identified as a combination of a narrow gas channel width a narrow contact rib width.

With respect to high-performance anode supported cells, the flowfield design on the cathode side adds up to 41% power loss, whereas the flowfield design on the anode side is of minor importance (<1% power loss).

References

[1] F. Tietz, V.A.C. Haanappel, A. Mai, J. Mertens, D. Stöver, J. Power Sources 156 (2006) 20–22.
[2] L. Blum, W.A. Meulenberg, H. Nabielek, R. Steinberger-Wilckens, Int. J. Appl. Ceram. Technol. 2 (2005) 482–492.
[3] M. Kornely, A. Neumann, N.H. Menzler, A. Leonide, A. Weber, E. Ivers-Tiffée, Proceedings of 9th European Solid Oxide Fuel Cell Forum, 2010, ch.7, pp. 70–76.
[4] W. Vielstich, H. Yokokawa, H.A. Gasteiger, Handbook of Fuel Cells, 6, John Wiley & Sons Ltd., 2009, pp. 921–931, Part 2.
[5] M.C. Tucker, H. Kurokawa, C.P. Jacobson, L.C. De Jonghe, S.J. Visco, J. Power Sources 160 (2006) 130–138.
[6] J.I. Gazzarri, O. Kesler, J. Power Sources 176 (1) (2008) 138–154.
[7] G.J. Nelson, C.L. Haynes, J. Power Sources 185 (2008) 1168–1178.
[8] C.W. Tanner, A.V. Virkar, J. Power Sources 113 (2003) 44–56.
[9] A. Leonide, V. Sonn, A. Weber, E. Ivers-Tiffée, J. Electrochem. Soc. 155 (2008) B36–B41.
[10] A. Leonide, S. Ngo Dinh, A. Weber, E. Ivers-Tiffée, Proceedings of the 8th European Solid Oxide Fuel Cell Forum, 2008, p. A0501.
[11] H. Schichlein, A.C. Müller, M. Voigts, A. Krügel, E. Ivers-Tiffée, J. Appl. Electrochem. 32 (2002) 875–882.
[12] V.A.C. Haanappel, A. Mai, J. Mertens, Solid State Ionics 177 (2006) 2033–2037.
[13] A. Weber, A.C. Müller, D. Herbstritt, E. Ivers-Tiffée, Proceedings of the Seventh International Symposium on Solid Oxide Fuel Cells (SOFC-VII), 2001, pp. 952–962.
[14] J. Kim, A.V. Virkar, K. Fung, K. Mehta, S.C. Somghal, J. Electrochem. Soc. 146 (1) (1999) 69–78.